Fourth International Symposium on Marine Propulsors
smp'15, Austin, Texas, May-June 2015

Marine propeller acoustic modelling: comparing CFD results with an acoustic analogy method

Thomas Lloyd[1,2], Douwe Rijpkema[3], Erik van Wijngaarden[3]

{t.lloyd; d.r.rijpkema; h.c.j.v.wijngaarden}@marin.nl

[1] MARIN Academy, Wageningen, The Netherlands; [2] Visiting Researcher, University of Southampton, Southampton, U.K.;
[3] MARIN, Wageningen, The Netherlands

ABSTRACT

Propeller noise and vibration is important in the design of ships in order to improve comfort, reduce signature or mitigate environmental impact. Since acoustic measurements are often difficult to perform in typical maritime experimental facilities, acoustic predictions based on computations are attractive. We utilised an acoustic analogy method to make acoustic predictions based on post-processing of a hydrodynamic simulation. Grids were designed to improve the resolution of the pressure field away from the propeller. This was then used as a comparison for the acoustic analogy method.

The local pressure at a field point was shown to be more sensitive to grid refinement than integrated propeller performance coefficients. Although the predictions made using the acoustic analogy in general agree well with the directly computed pressure, the method also suffers from sensitivity to the required input data (pressure, velocity and acceleration). For a probe located further away from the propeller, where the pressure amplitudes are smaller, numerical disturbances are seen, which could affect predictions, especially when higher frequencies are of interest. This highlights the need for a well-converged accurate hydrodynamic solution when using an acoustic analogy method.

Visualisation of the acoustic sources not only confirms the dominant noise-generating effects but also allows the spatial distribution of the acoustic sources to be examined. This may be useful for future noise reduction studies.

Keywords

hydroacoustics; propeller noise; CFD; acoustic analogy; pressure pulses

1 INTRODUCTION

Marine propeller noise and vibration has typically been studied in order to reduce the acoustic signature of naval vessels, or to improve comfort onboard passenger vessels. More recently, an emphasis has been placed on the impact of maritime noise on the environment, with the aim of reducing acoustic radiation from merchant shipping. Therefore the importance of acoustic measurements and simulations during design development has increased.

A key advantage of acoustic simulations is the freedom provided in the placement of probes (hydrophones), which may be somewhat restricted in typical experimental environments. In addition, experimental pressure sensors may measure facility reverberations and/or model vibrations, which are subsequently difficult to separate from the recorded signals. Some of these issues are addressed by Felli et al. (2014), for example. Simulations have previously examined how scale effects (Schuiling et al., 2011) and propeller geometry (Paik et al., 2013) can influence hull pressure fluctuations.

Numerical predictions of propeller noise are not without difficulty however. The ability of a Navier-Stokes solution to resolve pressure fluctuations far away from the source may be questioned, especially since the incompressibility assumption is invoked in maritime simulations. Another challenge is to develop a suitable grid, since the required resolution is both frequency dependent and spatially non-uniform.

One alternative to directly evaluating the pressure field is the *acoustic analogy* approach. Commonly used in the aeroacoustics community, and now increasingly so within the maritime field, this family of methods removes the direct dependence of the far-field pressure signal on the hydrodynamic simulation. Instead, the acoustic sources are described by the Navier-Stokes solution, and the acoustic analogy used to propgate this information to chosen receiver locations. In this way evaluations can be made at locations where the Navier-Stokes pressure field does not permit accurate predictions (due to grid coarseness or close proximity to boundaries), or outside of the computational domain itself. Studies of this type are not common however, due to the limited availability of validation data.

In this paper, we evaluate the predictive capabilities of an acoustic analogy method for receivers located inside the computational domain, permitting comparison to the Navier-Stokes solution. In §2, we outline the key details of the numerical approach. Next, an overview of the test case setup is given, in §3. The results are divided into two main

sections, namely steady simulations in §4, and unsteady in §5. Finally, discussion and conclusions are made in §7.

2 NUMERICAL APPROACH

2.1 Hydrodynamic solution

We solved the governing flow equations using the computational fluid dynamics (CFD) code *ReFRESCO*®, developed by MARIN in collaboration with various universities worldwide, and previously validated for complex propulsor configurations (Rijpkema & Vaz, 2011). The code adopts a finite volume face-based approach, permitting the use of grid cells with an arbitrary number of faces, which eases the gridding of complex engineering geometries. Flow variables are colocated at cell centres, and the equations coupled using a segregrated SIMPLE-type solution algorithm (Patankar, 1980). Parallelisation is achieved using Message Passing Interface and domain decomposition.

Numerous turbulence modelling approaches, cavitation models and numerical schemes are available; here we focus on details relevant to the present work. We performed wetted flow Reynolds-averaged Navier-Stokes computations, using the $k-\omega$ SST 2003 model for turbulence (Menter et al., 2003). Using this approach, all the turbulence is modelled. All flow variables were discretised in space using second-order schemes, except for the convective flux of the turbulence quantities which was treated using a first-order upwind scheme. Where used, time stepping was achieved using an implicit Euler (first-order) scheme.

Two approaches for reaching a converged periodic flow solution were employed. In the first, the equations are solved in a steady manner, with a final solution obtained after the residuals of the flow variables have reduced below a certain tolerance. Rotation is accounted for using the *absolute formulation*, whereby the velocity vector $\boldsymbol{U}$ is defined in the earth-fixed reference frame, while the equations are solved in the body-fixed reference frame, rotating with a grid velocity $\boldsymbol{U}_g = 2\pi n \times \boldsymbol{x}_g$. In these simulations, "time series" are extracted by artificially rotating the spatial solution relative to the defined probe locations.

Alternatively, the unsteady RANS equations are solved, requiring an explicit rotation of the grid within each time step. In this case, the equations are solved to the chosen residual tolerance for a given grid position, after which the grid is rotated to a new position and the process repeated. The time taken to achieve a periodic solution depends on numerous factors, such as grid density, initial conditions and advance ratio, but is typically $\mathcal{O}(L_x/U_0)$, where L_x is the domain length and U_0 the inflow speed. Based on a non-dimensional simulation time $T_x^* = nT_x \approx 11.4$, where T_x is the time for one domain flow-through, 12 propeller revolutions were used for all cases. The aim was to minimise transient effects caused by the boundary conditions, as well as allowing the propeller wake sufficient time to develop.

While the unsteady computations more closely represent reality, they are (sometimes prohibitively) slow due to the time taken to reach a periodic solution and high level of parallel communication between stationary and moving grid domains. Hence the steady solution method presents an advantage in terms of cost-saving, especially when many different cases must be simulated. We note however the limited applicability of the steady approach outside of purely open-water scenarios. Hence we present both approaches here, with the steady method used primarily for numerical testing, and the unsteady investigated with the intention of moving towards more complex propeller-hull interaction cases.

2.2 Hydroacoustic solution

Acoustic predictions were obtained using the Ffowcs Williams-Hawkings (FW-H) acoustic analogy (Ffowcs Williams & Hawkings, 1969). The original formulation is a rearrangement of the governing (compressible) flow equations into an inhomogeneous linear wave equation *i.e.* it describes the propagation of acoustic waves due to sources represented on the right-hand-side. The sources are described on some suitable surface, and may conveniently be provided from a CFD solution.

Numerous versions of the formulation exist. Here we provide brief details of the equation used in this work, which was formally derived by Di Francescantonio (1997):

- Acoustic sources are described on a porous data surface (PDS) surrounding the source region. This is suitable for hydroacoustics where the location of the sources is not necessarily known *a priori* as well as allowing for cavitation to be included inside the PDS. This contrasts with aeroacoustics applications where the blade surfaces themselves are typically used as the source locations.

- The non-linear "quadrupole" term, which was originally a volume integral, is re-formulated as a surface integral. This allows non-linear sources to be included without peforming expensive spatial derivatives and integrations.

- The "unsteady dipole" terms (those with $1/c_0 r$ dependence) are negligible in this case, since open-water conditions are treated, and will not be presented in the results.

- Free-field propagation of the sources has been assumed, since only open-water conditions have been considered here.

The solution for the acoustic pressure may be written as

$$4\pi p'(\boldsymbol{x},t)H(f) = \underbrace{\int_S \frac{\rho_0 \dot{u}_n}{r} dS(\boldsymbol{y})}_{\text{monopole, } p_0} + \underbrace{\int_S \frac{p\hat{\boldsymbol{n}}\cdot\hat{\boldsymbol{r}}}{r^2} dS(\boldsymbol{y})}_{\text{dipole, } p_1} + \underbrace{\int_S \frac{\rho_0 u_n u_r}{r^2} dS(\boldsymbol{y})}_{\text{non-linear dipole, } p_2} + \underbrace{\int_S \frac{\dot{p}\hat{\boldsymbol{n}}\cdot\hat{\boldsymbol{r}}}{c_0 r} dS(\boldsymbol{y}) + \int_S \frac{\rho_0 \dot{(u_n u_r)}}{c_0 r} dS(\boldsymbol{y})}_{\text{unsteady dipole}}, \quad (1)$$

where p' the acoustic pressure fluctuation at the receiver location $\boldsymbol{x}$ and H is the Heaviside function with $f = 0$ corresponding to the location of the PDS. The acoustic sources are located at $\boldsymbol{y}$ and integrated over S. The fluid density is denoted by ρ_0, velocity by $\boldsymbol{u}$, pressure by p and speed of sound by c_0. Time derivatives are indicated by $\dot{()}$. $r = |\boldsymbol{r}|$ is the source-receiver distance, $\hat{\boldsymbol{n}}$ and $\hat{\boldsymbol{r}}$ are the unit vectors in the normal and receiver directions respectively, and the subscripts n and r denote dot products with these unit vectors. Definitions are provided in Figure 1.

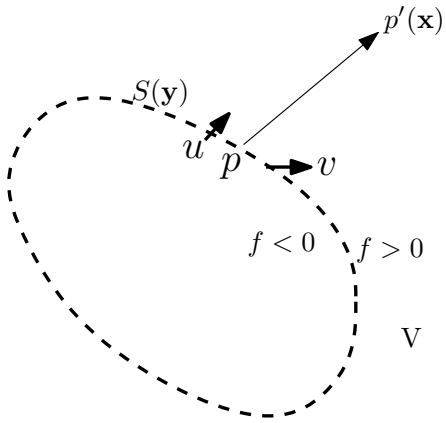

Figure 1: Schematic representation of acoustic analogy porous data surface and associated definitions.

Equation 1 has been implemented into *ReFRESCO* as a post-processing module. Data are interpolated onto the PDS from the flow solution, and files written containing both source description and radiated pressures. Since the individual terms of Equation 1 can be related to physical mechanisms of noise generation, it is useful to analyse their contributions to the total pressure signal, as has been carried out in §5.

3 TEST CASE DESCRIPTION

3.1 Case overview

The propeller considered in this work was the INSEAN E779A, which is widely used for computational test cases due to the availability of large amounts of experimental data (see *e.g.* Salvatore, 2007). Particulars of the case are summarised in Table 1. Only open water conditions were considered. The advance ratio is defined as

$$J = \frac{U_0}{nD_P}. \quad (2)$$

Table 1: Details of E779A propeller test case

parameter	symbol	value	unit
no. of blades	Z	4	-
propeller diameter	D_P	0.227	m
rotation rate	n	25	Hz
inflow speed	U_0	5	ms^{-1}
advance ratio	J	0.88	-

This case corresponds to that studied by Ianniello et al. (2013), who used a Navier-Stokes solver in combination with the Ffowcs Williams-Hawkings equation to make acoustic predictions. We aimed to replicate this case setup and compare to these authors' results, due to the fact that no experimental acoustic measurements are available for the E779A propeller in open water.

3.2 Domain design

A representation of the domain, including boundary conditions and probe locations, is given in Figure 2. It was designed to replicate open-water conditions, with flow in the negative x-direction and an infinite shaft extending through the propeller wake to the outlet.

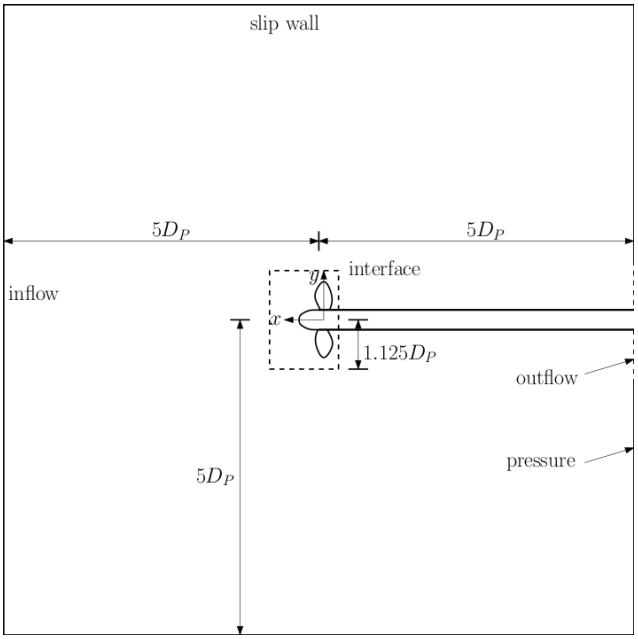

Figure 2: Schematic representation of simulation domain: slice at $z = 0$. Approximately to scale.

Boundary conditions are summarised in Table 2. At the outlet, a mixed outflow/pressure boundary was specified. In our experience this significantly reduces artificial reflection of the propeller wake, which can lead to low-frequency

oscillations throughout the domain. The interface boundary serves two main purposes: it allows the inner domain to rotate within the outer domain during unsteady simulations; and, it provides a general method for coupling two non-conformal domains. The reason for this is explained in Section 3.3.

Table 2: Summary of boundary conditions

boundary	velocity	pressure
inflow	$(u, v, w) = (U_0, 0, 0)$	$\partial_n p = 0$
outflow	$\partial_n(u, v, w) = 0$	$\partial_n p = 0$
pressure	$\partial_n(u, v, w) = 0$	$p = 0$
farfield	$u_n = 0$	$\partial_n p = 0$
blades and shaft	$u_n = 0$	$\partial_n p = 0$
interface	nearest cell interpolation	

3.3 Grid generation

For this study, a set of geometrically similar block structured grids were generated, in order to allow uncertainty analyses to be performed. A modified approach was taken from that typically used for propeller open-water simulations. At MARIN, the structured grid generator *Gridpro*® has been found to create high quality grids, particularly close to solid boundaries. An advantage of this package is its optimisation engine, which generally results in grids with smooth stretching and low skewness, which is important for structured gridding of complex geometries such as propellers. However, this automation removes some of the control from the user, presenting a drawback when grid quality away from the propeller should be closely controlled (as is the case for hydroacoustics).

In order to achieve this we generated an outer domain using *Pointwise*® to create a simplified block topology, particularly focussing on the cell distribution in the region of the hydrophone locations. Here an almost uniform cell size was sought, in order to try and reduce the numerical diffusion affecting the pressure signals at the probes. This approach also minimises pressure disturbances induced by the absolute formulation (steady simulations). Views of an example grid are shown in Figure 3. Table 3 summarises the total cell count for all grids.

Table 3: Approximate cell counts (N; millions of cells) and time steps ($\Delta\theta$; degrees) for all grids .

grid	N	$\Delta\theta$ / °	grid	N	$\Delta\theta$ / °
2	27.1	0.33	5	3.1	0.64
3	13.2	0.41	6	1.4	0.80
4	7.3	0.51	7	0.6	1.00

3.4 Porous data surface design

The PDS dimensions were chosen to replicate those of Ianniello et al. (2013), who used an open-ended cylinder surrounding the propeller and wake. This is justified as long as the line of sight between the acoustic sources and the probe location intersects the PDS (Freund et al., 1996). A diameter of $1.25D_P$ was used, meaning the PDS was situated outside the interface between the two grid domains, and in a region of uniform grid density. This was expected to improve the interpolation of hydrodynamic variables onto the PDS. The surface length was $3D_P$. We based the panel density of the PDS on our previous investigations (van Wijngaarden & Rijpkema, 2012; **?**). The number of axial and circumferential panels used was 70 and 180 respectively. A view of the PDS and probe locations is given in Figure 4.

4 PERFORMANCE PREDICTION

4.1 Solution convergence

For the steady simulations all six grids listed in Table 3 were used. In general, all flow variables were converged to an L_∞ norm of at least 10^{-5}. For the finest grid, the turbulence dissipation ω did not converge to this level; this was not expected to affect the pressure solution however.

The probe positions (Figure 4) were chosen as representative of typical locations where hull pressures may be measured. They were also selected to allow investigation of the effect of radial distance from the propeller on the pressure field.

For the unsteady simulations time step and grid dependence studies were performed simultaneously, by maintaining an approximately constant Courant number between all grids. A time step equivalent to a rotational increment of one degree was used for the coarsest grid (grid 7); in our experience this value proves sufficient temporal resolution for unsteady wetted flow cases. For each of the subsequent finer grids, the time step was reduced by the same factor as the grid refinement ratio (0.8). Due to the high computational cost, no unsteady results were obtained for grid 2.

It is important to note that it is typically not possible to converge unsteady simulations to the same accuracy as when the absolute formulation is used. In the following results, an L_2-residual of 10^{-5} was achieved, while the L_∞-residual was typically two orders of magnitude higher than for the steady results.

4.2 Performance coefficients

Propeller performance coefficients (thrust, torque and open-water efficiency) are given in Table 4, along with the pressure pulse coefficient K_p which is the non-dimensionalised pressure amplitude at the chosen probe locations. These are defined as

$$K_T = \frac{T}{\rho_0 n^2 D_P^4}; \quad K_Q = \frac{Q}{\rho_0 n^2 D_P^5};$$
$$\eta_0 = \frac{K_T J}{2\pi K_Q}; \quad K_p = \frac{p}{\rho_0 n^2 D_P^2}; \tag{3}$$

where T and Q are the propeller thrust and torque respectively.

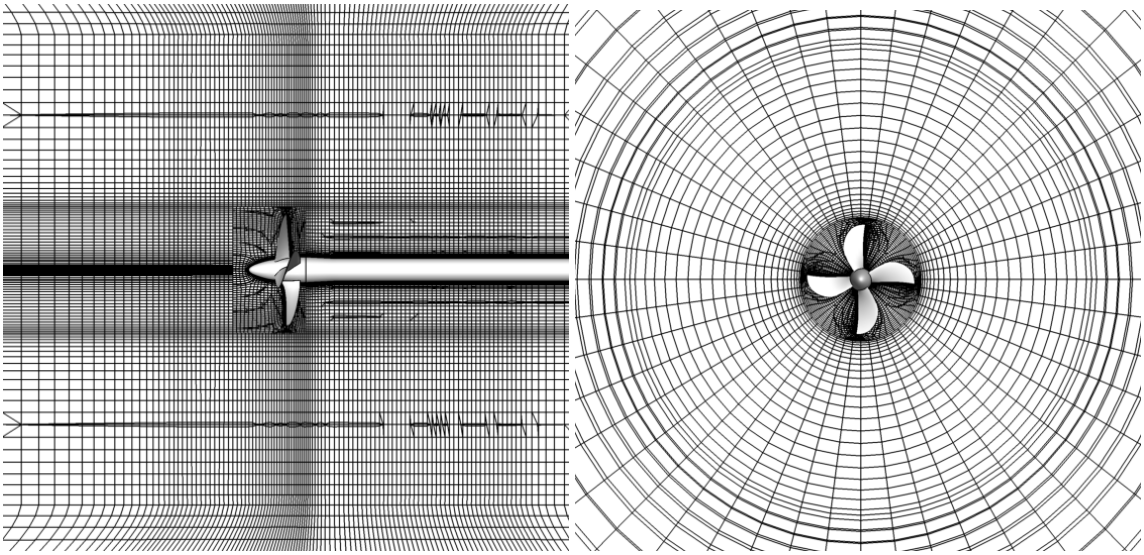

Figure 3: Vertical ($z = 0$; left) and propeller plane ($x = 0$; right) slices of grids. Coarse grid shown.

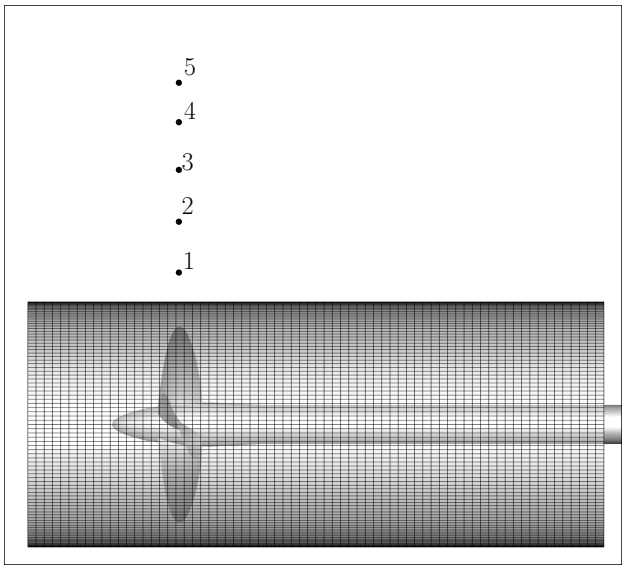

Figure 4: Side view of porous data surface and probe locations. All probes lie on the plane $y = 0$, and are spaced from $1.3D_P - 2.3D_P$ relative to the global origin. Probe 5 has the same location as used by Ianniello et al. (2013).

Almost monotonic convergence of the peformance coefficients is seen for both steady and unsteady simulations, with differences in thrust and torque of only a few percent between the coarest and finest grids.

The values from the unsteady simulations are also seen to be very similar to the steady, which provides a degree of confidence in the convergence of the forces. For grid 3, the values are almost exactly the same.

4.3 Uncertainty analysis

The effect of grid sensitivity may be quantified by making an estimate of the numerical uncertainty. Here we used the method fully described in Eça & Hoekstra (2014), and do not include full details here. Briefly the method consists of:

- Computing results using four or more geometrically similar grids. This allows a Richardson extrapolation and least-squares fit of the results to be made.
- Estimating the error between a quantity from a given grid, and the exact (or best available) solution.
- Obtaining the order of convergence (β) of the least-squares fit.
- Computing the numerical uncertainty (U_ϕ) as the product of a safety factor and the estimated error. For $0.5 \leq \beta \leq 2.1$, the safety factor is 1.25.

Results of this analysis are presented in Table 4. Clearly the numerical uncertainty of the performance coefficients (K_T, K_Q and η_0) is very low. This is not the case for the chosen probe locations however, where a higher uncertainty is seen with increasing distance from the propeller. The difference in uncertainty highlights the increased difficulty in accurately predicting field values compared to integrated quantities.

Note that the uncertainty analysis was not carried out for the unsteady simulations since this requires a greater number of grid/timestep combinations to be computed. Although outside the scope of this study, we will pursue this as part of future work.

5 PRESSURE PULSE ANALYSIS

Harmonic analyses were performed on these signals using python™, by applying a Kaiser-Bessel windowing function, and a fast Fourier transform routine. Data were sampled at the Nyquist frequency, which removed some high-frequency numerical noise. The Kaiser-Bessel windowing function was chosen since it is known to provide good amplitude preservation and reduced spectral leakage.

Table 4: Summary of performance coefficients predicted by steady and unsteady simulations. First harmonic pressure amplitudes from steady simulations also shown. Values of K_p are shown for probes 1-3, and have been multiplied by 10^{-3}. Experimental values 'exp' obtained from curve fit of propeller open water thrust and torque measurements (Salvatore, 2007).

	steady						unsteady		
grid	K_T	$10K_Q$	η_0	K_p (1)	K_p (2)	K_p (3)	$\overline{K}_T$	$10\overline{K}_Q$	$\overline{\eta}_0$
2	0.1443	0.2926	0.6906	-	-	-	-	-	-
3	0.1445	0.2931	0.6905	5.58	2.91	1.61	0.1445	0.2937	0.6891
4	0.1450	0.2941	0.6905	5.64	2.96	1.64	0.1447	0.2940	0.6893
5	0.1463	0.2977	0.6880	5.87	3.05	1.74	0.1460	0.2975	0.6871
6	0.1480	0.3026	0.6851	5.64	3.00	1.67	0.1474	0.3017	0.6841
7	0.1481	0.3091	0.6710	5.92	3.03	1.83	0.1490	0.3103	0.6724
β	2.0	2.0	2.0	1.0	1/2	0.75			
U_ϕ	1.4	2.1	0.6	22.5	33.5	44.1			
exp	0.151	0.305	0.718	-	-	-			

We start by comparing results at probe 2 for both steady and unsteady simulations. This probe location is in fact very close to the propeller, where an acoustic method would not normally be considered necessary. However this allows verification of the FW-H method, which can then be used with greater confidence at larger receiver distances where no RANS comparison data is available.

Figure 5 presents a harmonic analysis of the pressure time traces, which are included as insert figures for each plot.

A generally good agreement is observed between the FW-H and RANS pressure signals. There are several key observations about these results however. We notice that the FW-H results are in general more sensitive to grid refinement than the RANS for the steady cases. The discrepancy between the two data sets is greatest on the coarest grid plotted here (grid 5). As might be expected the FW-H equation is sensitive to grid refinement, since the input quantities include not only the pressure but also velocity and velocity time derivatives.

The unsteady cases show the most consistent trend in terms of the change in the pressure amplitudes with grid refinement. We might expect this, since these simulations resolve the flow field in a more physically accurate way. The steady results for grid 3 however do show a very close agreement with the unsteady (Figure 5c), suggesting grid refinement plays a more important role. This is attributed to the fact that in the steady case the time derivative in the monopole term of Equation 1 is approximated by a spatial derivative.

Next, focussing on grid 3, we plot the individual terms from the FW-H equation contributing to the total pressure signal. Figure 6 shows this for steady and unsteady cases. The signal at this location is seen to be dominated by the linear terms (p'_0 and p'_1), which are of almost equal magnitude and phase. This is due to the close proximity of the probe to the PDS, as shown in **?**. Hence these terms no longer represent 'thickness' and 'loading' effects in the usual sense.

The small contribution from the nonlinear term (p'_2) was expected at this location, since in the propeller plane the blade dynamics dominate over the nonlinear flow effects of the wake. However, at this location close to the propeller, p'_2 is seen to be non-negligible. This has been identified as a source of discrepancy between the FW-H and RANS signals shown previously.

Hence in Figure 7 we perform the analysis previously shown in Figure 5c, plotting only the linear FW-H terms. Although the original agreement between the signals was in fact satisfactory, Figure 7 shows an improvement in the comparison for both steady and unsteady cases. This highlights that the FW-H equation is sensitive to probe location, since we would not expect a large contribution from p'_2 here. Including this term is however expected to be more significant for probe locations downstream of the propeller for non-cavitating conditions. We also emphasise that the relative magnitudes of the different FW-H terms will have some sensitivity to

Finally in this section, we show results at probe 5, located $2.3D_P$ above the propeller, where we can compare to the results of Ianniello et al. (2013). This has been performed to provide further confidence in our predictions since no experimental data are available. In this case, it is the unsteady results which show the closest agreement between the three data sets. The FW-H result is also closer to the comparison value than the RANS pressure.

An important observation however is that the unsteady signals (both FW-H and RANS) appear to suffer from some numerical disturbances, and are not fully periodic. These may be attributed to the sliding interface or pressure correction method used in the unsteady simulations. Although these were not seen for probe 2, where the pressure amplitudes are much greater, this highlights the need to obtain an accurate hydrodynamic solution in order to make pressure predictions further away from the propeller.

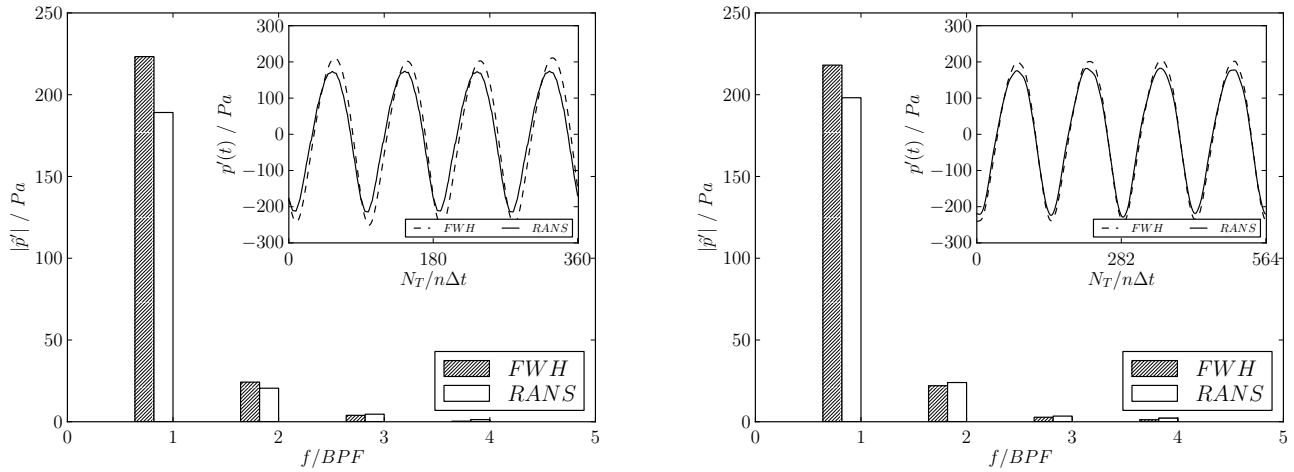

(a) grid 5

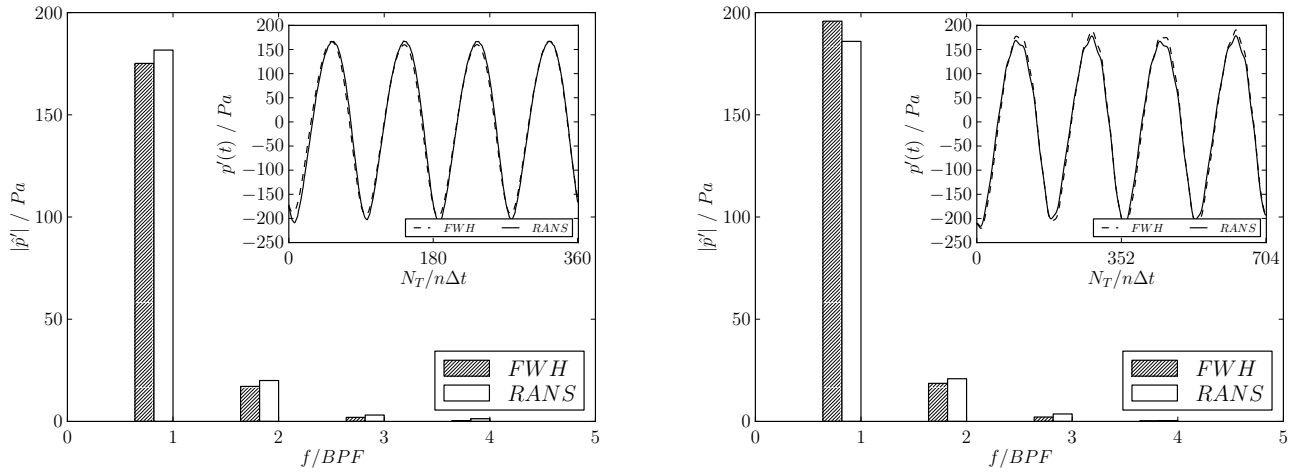

(b) grid 4

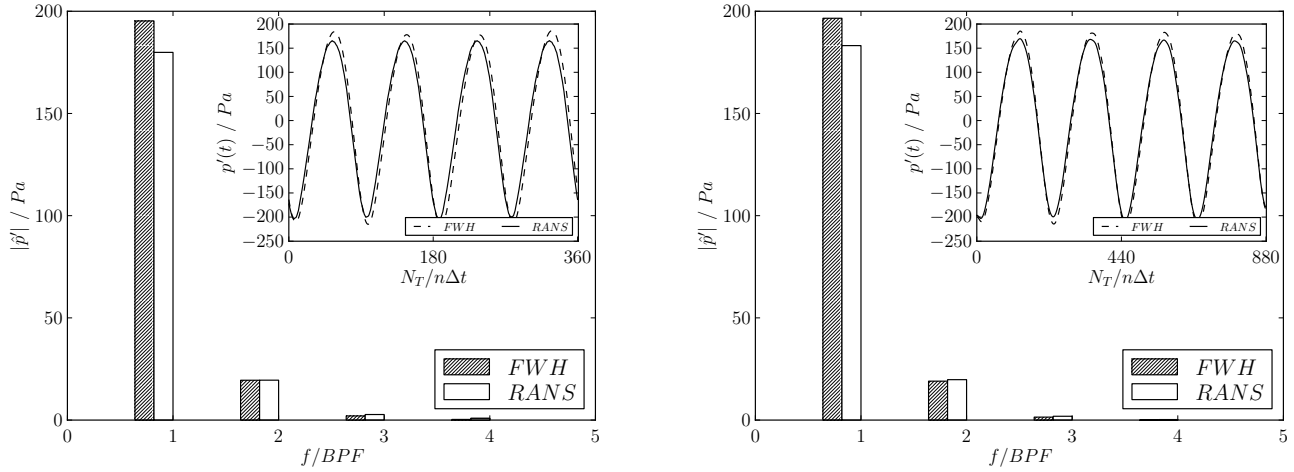

(c) grid 3

Figure 5: Hydroacoustic results for probe 2 from grids 5, 4 and 3: steady (left) and unsteady (right). N_T is the number of periods sampled.

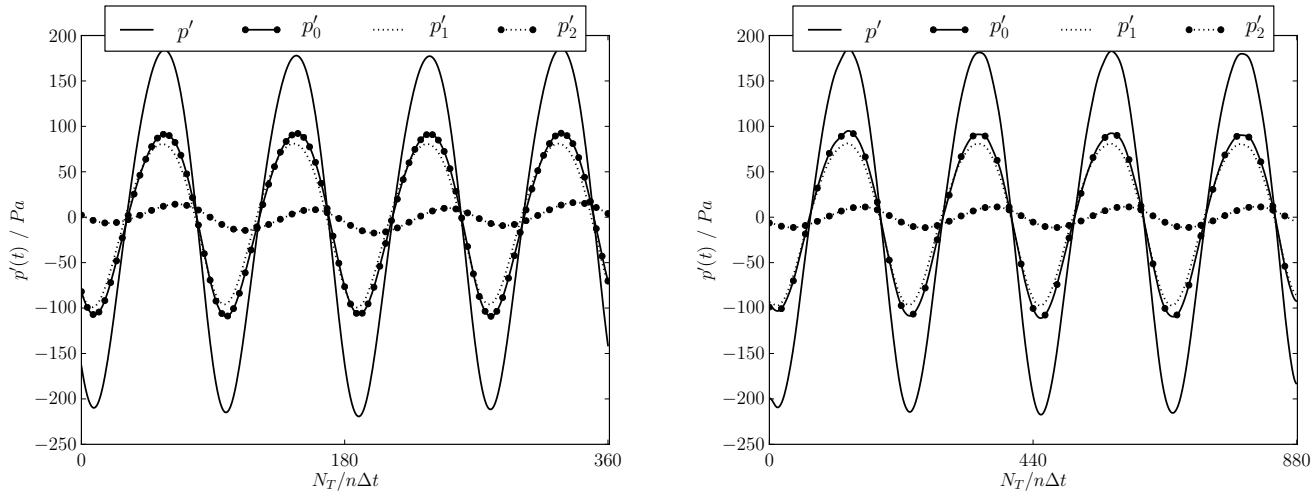

(a) steady (b) unsteady

Figure 6: FW-H equation terms extracted from grid 3.

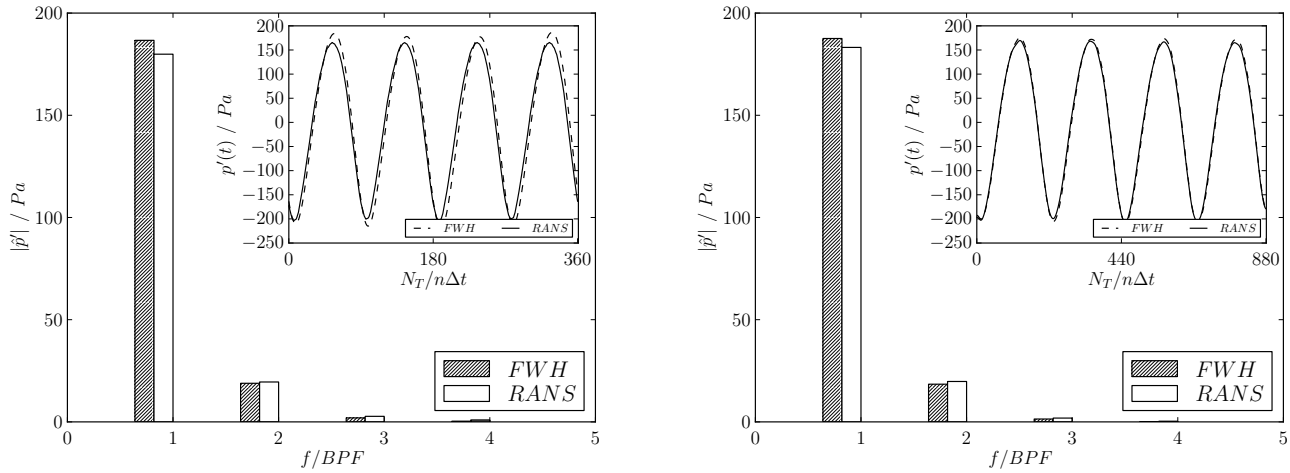

(a) steady (b) unsteady

Figure 7: Comparison between FW-H and RANS pressures at probe 2, using only linear components of FW-H equation ($p' = p'_0 + p'_1$).

6 ACOUSTIC SOURCE ANALYSIS

An advantage of using the FW-H equation over the RANS pressure is the additional information available about the location of the acoustic sources. Figure 9 shows the contribution to the first three terms in Equation 1, from each panel of the porous data surface. The intention is to highlight the spatial distribution of the source terms; their relative magnitudes cannot be compared in this figure since the pressure fluctuation is derived using the spatially-integrated time-averaged pressure (*e.g.* $p'_0 = p_0 - \bar{p}_0$).

We observe a relatively limited spatial extent of the acoustic sources (particularly the monopole term). It is known from propeller acoustic theory that the blade thickness effect is concentrated close to the propeller plane (Goldstein, 1976). The dipole and non-linear terms have a higher axial distribution, confirming that the PDS should extend upstream a sufficient distance to include these effects accurately. The hydrodynamics of the wake flow are not observed on the PDS, and hence their contribution is not easily elucidated. However since for non-cavitating flow the pressure fluctuations rapidly reduce downstream of the propeller, these effects may not in general be as important to capture.

The dominance of the propeller pressure field over that in the wake is corroborated in Figure 10a, where a slice of the pressure at $y = 0$ is presented, with the tip vortex visualised using the 'Q-criterion', which identifies regions of strongly rotating flow. For a probe location further downstream and

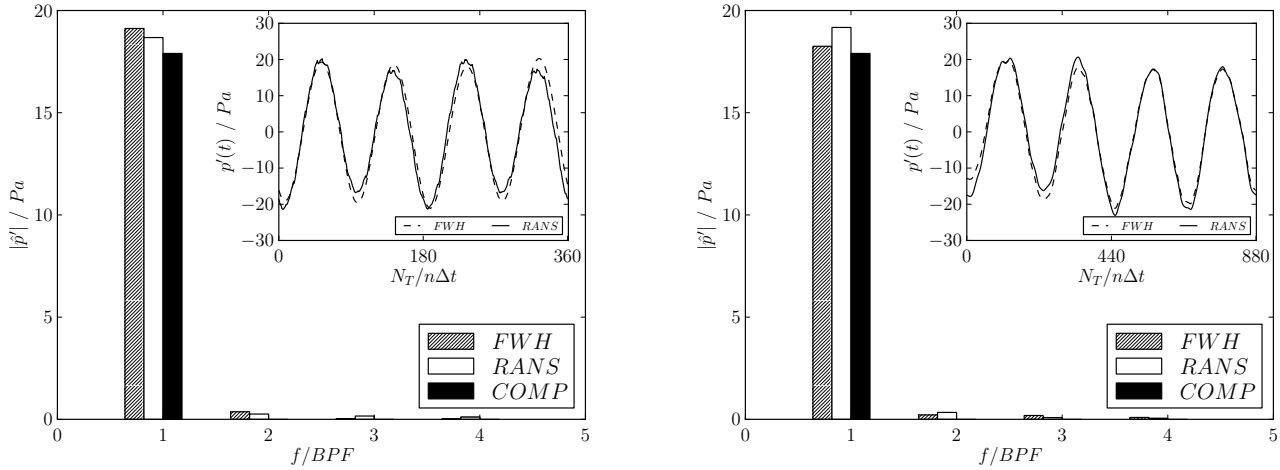

(a) steady

(b) unsteady

Figure 8: Predicted pressures at probe 5 from grid 3: comparison between FW-H, RANS and value taken from Ianniello et al. (2013).

close to the wake, the non-linear contribution from the tip vortex may become stronger. The relevance of this is questionable however, given that the pressure amplitude here would be much lower than directly above the propeller, and this probe location is unrealistic for hull pressure or radiated noise studies.

Figure 10 also provides some confidence in the unsteady simulation, by visual inspection of the flow field. Despite the fact the steady simulation has been converged to a lower residual value, the results appear qualitatively very similar. It is particularly important in unsteady simulations to minimise the influence of the sliding interface (shown here in black) on the downstream propogation of the tip vortex. In Figure 10a, the vortex closely resembles that from the steady case where no explicit rotation of the grid domains takes place.

The main difference is the splitting of the tip vortex further upstream in the unsteady case, although the resulting structure propagates downstream with less dissipation than for the steady simulation. The pressure distribution on the pressure side of the blades is also very similar, as seen in Figure 10b. This also manifests in the identical prediction of the thrust coeffcient for these two cases, as shown in Table 4.

7 CONCLUDING REMARKS

This paper has presented a preliminary study of propeller hydroacoustics and use of an acoustic analogy method. The findings may be summarised by the following:

- Typical propeller grids may not be entirely suitable for predicting pressure fluctuations at probe locations far from the propeller, since the grid is normally not locally refined here. Modifications to achieve a more uniform grid distribution in the region of the probes may be necessary.
- Predicting the local pressure at a field point directly from a RANS computation is challenging, with the pressure exhibiting much higher uncertainty than the integrated propeller performance coefficients.
- The Ffowcs Williams-Hawkings acoustic analogy method compares well with the direct RANS pressure for probes in the propeller plane. The FW-H equation is however seen to be more sensitive to the accuracy of the input data, and hence a fine grid should be used to compute the required hydrodynamic inputs.
- The role of the nonlinear term in the FW-H equation is not fully understood. For probes used here it gives an apparently spurious contribution to the total pressure signal. Although it may become more important for other probe locations, we do not expect this to be important for cavitating conditions, where the monopole term is likely to have a much higher amplitude.
- Both the integrated and local data surface contributions to the terms of the FW-H equation can be visualised in order to help identify dominant noise sources, providing additional information not available from the direct pressure signal.

Future work should consider, amongst other areas, a full uncertainty analysis of unsteady computations, for a larger number of grid and timestep combinations. Following this it will also be useful to examine the effect of changing the dimensions and location of the porous data surface, as well

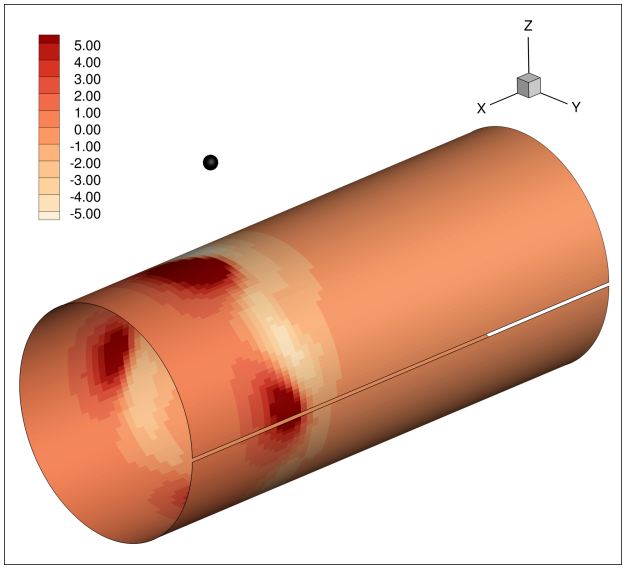

(a) $p_0 \,/\, m^{-2}$

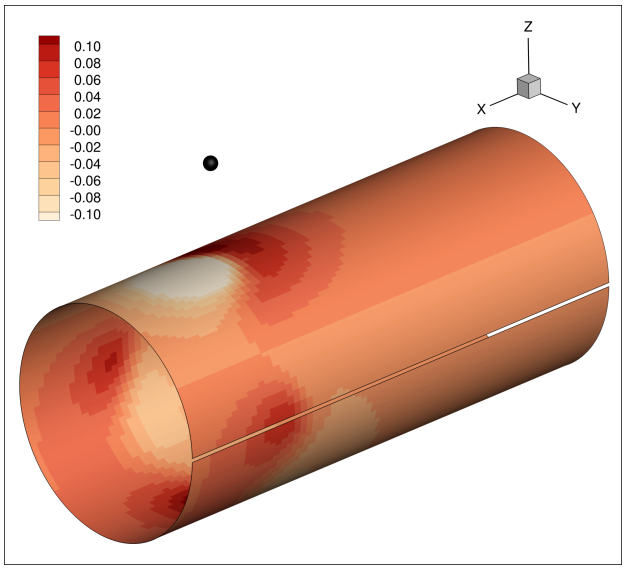

(b) $p_1 \,/\, m^{-2}$

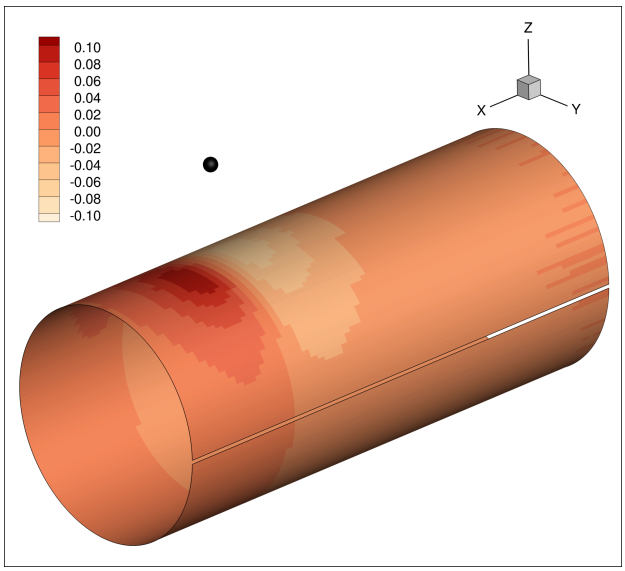

(c) $p_2 \,/\, m^{-2}$

Figure 9: Ffowcs Williams-Hawkings equation source terms per panel for probe $U2$. Probe location shown as black sphere.

as comparing the pressure signals at a wider range of receiver locations in order to determine when best to use the acoustic analogy method.

ACKNOWLEDGEMENTS

The financial support of the MARIN Academy is gratefully acknowledged. Computational resources were provided by the Iridis4 and Marclus4 HPC clusters.

REFERENCES

Di Francescantonio, P., 1997. 'A new boundary integral formulation for the prediction of sound radiation'. Journal of Sound and Vibration, **202**(4), pp. 491–509.

Eça, L. & Hoekstra, M., 2014. 'A procedure for the estimation of the numerical uncertainty of CFD calculations based on grid refinement studies'. Journal of Computational Physics, **262**, pp. 104–130.

Felli, M., Falchi, M. & Dubbioso, G., 2014. 'Direct and indirect experimental methodologies for the hydroacoustic analysis of marine propellers'. Proceedings of the 30th Symposium on Naval Hydrodynamics. 2nd-7th November, Hobart.

Ffowcs Williams, J. E. & Hawkings, D. L., 1969. 'Sound generation by turbulence and surfaces in arbitrary motion'. Philosophical Transactions of the Royal Society A: Mathematical, Physical and Engineering Sciences, **264**(1151), pp. 321–342.

Freund, J. B., Lele, S. K. & Moin, P., 1996. 'Calculation of the radiated sound field using an open Kirchhoff surface'. AIAA Journal, **34**(5), pp. 909–916.

Goldstein, M. E., 1976. Aeroacoustics. McGraw-Hill, New York.

Ianniello, S., 2014. 'The underwater noise prediction from marine propellers: an essentially nonlinear problem'. Proceedings of the 21st International Congress on Sound and Vibration. 13-17 July, Beijing, pp. 1–8.

Ianniello, S., Muscari, R. & Mascio, A., 2013. 'Ship underwater noise assessment by the acoustic analogy. Part I: nonlinear analysis of a marine propeller in a uniform flow'. Journal of Marine Science and Technology, **18**(4), pp. 547–570.

Lloyd, T. P., Lidtke, A. K., Rijpkema, D. R., Wijngaarden, E. V., Turnock, S. R. & Humphrey, V. F., 2015. 'Using the Ffowcs Williams-Hawkings equation for hydroacoustics of propellers'. Proceedings of the 18th Numerical Towing Tank Symposium. 28th-30th September, Cortona.

Menter, F. R., Kuntz, M. & Langtry, R., 2003. 'Ten Years of Industrial Experience with the SST Turbulence Model'. Turbulence, Heat and Mass Transfer.

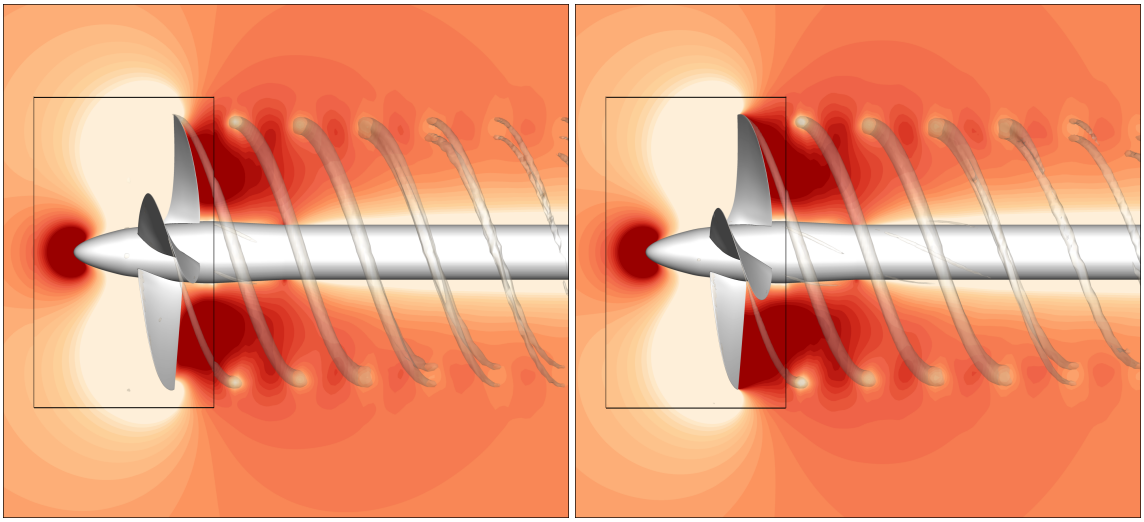

(a) Tip vortex and near-field pressure: iso-surface of $Q = 1s^{-1}$; $y = 0$ slice of $K_p = -0.03$ (light) to 0.03 (dark). Location of sliding interface indicated by solid black lines.

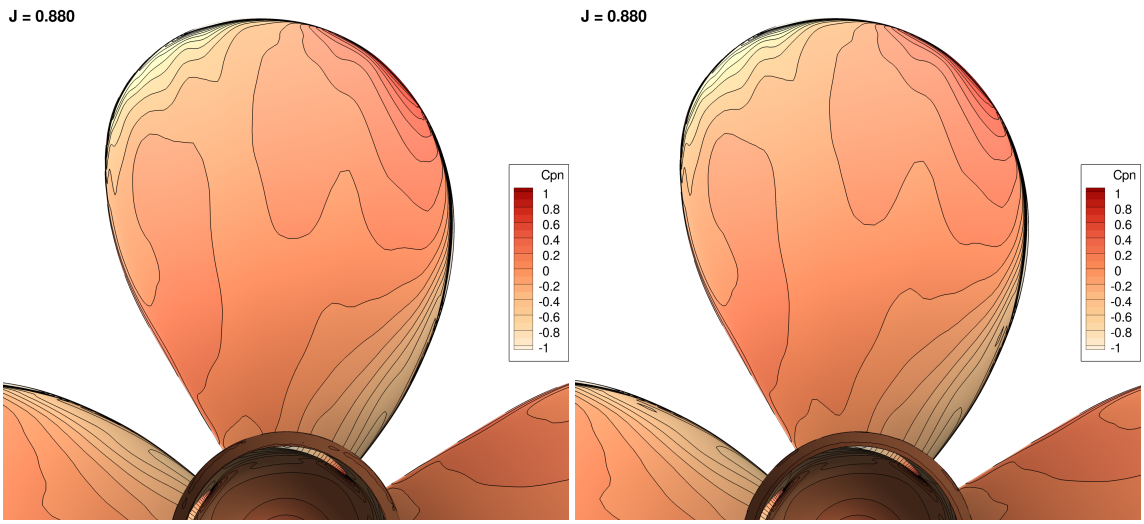

(b) blade surface pressure: $C_{pn} = \frac{2(p-p_0)}{\rho_0(nD_P)^2}$

Figure 10: Visualisation of the tip vortex and pressure field for simulations using grid 3: steady (left) and unsteady (right).

Paik, K.-J., Park, H.-G. & Seo, J.-S., 2013. 'URANS simulations of cavitation and hull pressure fluctuation for marine propeller with hull interaction'. Proceedings of the 3rd International Symposium on Marine Propulsors. 5th-7th May, Launceston, pp. 389–396.

Patankar, S., 1980. Numerical heat transfer and fluid flow. McGraw-Hill, New York.

Rijpkema, D. R. & Vaz, G., 2011. 'Viscous flow computations on propulsors: verification, validation and scale effects'. Proceedings of Marine CFD. London.

Salvatore, F., 2007. 'The INSEAN E779A propeller experimental dataset'. Tech. rep., INSEAN, Report No. D4.1.3.

Schuiling, B., Lafeber, F. H., van der Ploeg, A. & van Wijngaarden, E., 2011. 'The influence of the wake scale effect on the prediction of hull pressures due to cavitating propellers'. Proceedings of the 2nd International Symposium on Marine Propulsors. 15th-17th June, Hamburg, pp. 124–131.

van Wijngaarden, E. & Rijpkema, D. R., 2012. 'Coupling a Helmholtz-equation hydroacoustic model and CFD solvers'. Tech. rep., MARIN.

DISCUSSION

Question from Mario Felli

Have the authors analysed the relative decay of the linear and non-linear terms of the FW-H [equation] with distance? In particular, I am [interested] to know if the non-linear term dominates the acoustic pressure fluctuations in the farfield as shown in Ianniello et al. (2013).

Authors' closure

Thank you for your question, which raises an interesting point about the role of the non-linear sources. Using the data already presented here, we show the relative magnitudes of the first harmonic for FW-H equation terms between probes 5 and 2. These are summarised in Table 5.

Table 5: Relative magnitudes of first harmonic FW-H equation terms between probes 5 and 2.

term	value
$p'^{\{5/2\}}$	0.094
$p_0'^{\{5/2\}}$	0.093
$p_1'^{\{5/2\}}$	0.102
$p_2'^{\{5/2\}}$	0.017

This example clearly illustrates that the non-linear term decays *faster* than the linear terms, at this axial location (directly above the propeller). This result confirms the rapid decay of marine propeller noise with distance (as shown by Ianniello (2014)), but not that the non-linear term becomes more important in the farfield. This conclusion may not be true for other probe locations however, particularly those close to the propeller wake, where the blade loading and thickness effects should be much smaller. In this case we expect to see a larger contribution from the non-linear term (see our more recent paper (Lloyd et al., 2015)), but have not looked at the effect of the radial distance on the relative contributions. This will be included in future work.

Questions from Emre Güngör

Would it be better to perform some additional test cases not only to see the correct acoustic wave [in] the farfield but also just [in] the nearfield? [Have] you had a chance to [perform] some test cases on simple geometries? Could you please [explain] how you could separate the monopole and dipole contributions to the total pressure amplitude with respect to frequency?

Authors' closure

Thank you for your questions. in order to answer your first two questions, we have already performed computations using simple monopole and dipole source descriptions. See for example Lloyd et al. (2015). Here we show the time trace for a dipole source of amplitude 1 Pa, compared to the analytical solution (Figure 11).

Using this approach we are able to rapidly verify the code implementation as well as sensitivity of the acoustic predictions to the setup of the porous data surface.

Your last question concerns separating contributions of the various source terms to the total pressure signal. We do this by post-processing the signals of the individual source terms into harmonic amplitudes, along with accompanying phases. Table 6 illustrates this for the first harmonic of probe 2, where the phase is defined as a lag relative to the blade TDC position.

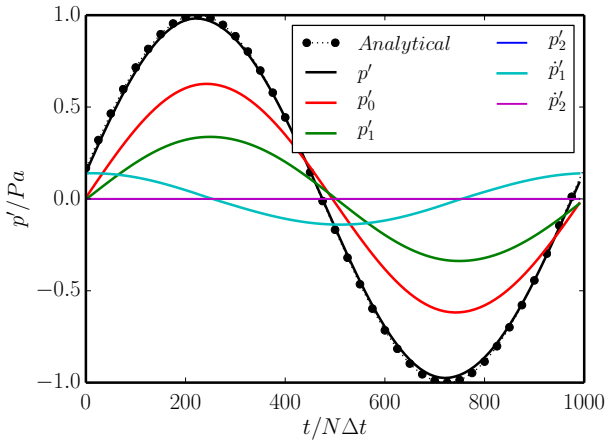

Figure 11: FW-H prediction of pressure due to dipole source, compared to analytical solution: relative integrated contributions from each acoustic analogy source term for frequency $n = 100\ Hz$ and receiver at $|\mathbf{r}| = 1\ m$. Maximum pressure amplitude is $|p'| = 1\ Pa$.

Table 6: Contributions to the first harmonic farfield pressure from the FW-H source terms at probe 2.

term	amp / Pa	phase / deg
p'	196.6	152.9
p_0'	99.5	153.4
p_1'	88.1	156.0
p_2'	11.5	115.1

In this case, it can be seen that the phase difference between the total signal and the linear terms is small, while the non-linear term shows a phase lead. This is confirmed by examining Figure 6b.